Accuracy of a slew maneuver for the HYPSO-1 satellite – in-orbit results*

Bjørn A. Kristiansen[1,†], Dennis D. Langer[2,†], Joseph L. Garrett[1], Simen Berg[1], J. Tommy Gravdahl[1], Tor A. Johansen[1]

***Abstract*— In this paper, the accuracy of a slew maneuver performed by the HYPSO-1 satellite is analysed based on the data received during the satellite's first months in orbit. The slew maneuver, during which the satellite turns with a constant angular velocity over a given target area, is meant to decrease the ground sampling distance of pixels recorded by the push-broom hyperspectral imager. We compare the pointing accuracy when pointing nadir with the accuracy the satellite achieves when the satellite slews, and also the impact the slew maneuver has on the resulting data products, namely the decreased ground sampling distance and the increased signal per area. The selected slew maneuver itself shows a root-mean-square accuracy of 0.675 mrad/s about the axis of rotation. Analysis of the images shows that the slew maneuver provides 2.80 times as many samples per area, and a decrease in ground sampling distance of 63.6% along track.**

***Index Terms*— slew maneuver, attitude control, push-broom imaging, ground sampling distance, hyperspectral**

I. Introduction

During a slew maneuver, the body, in this paper a satellite, rotates with a constant angular velocity relative to some frame. This is in contrast to point-to-point maneuvers, otherwise called pointing maneuvers or set-point regulation. Various papers discuss the slew maneuver in theory, see for example [1], [2], [3], [4], and [5]. Possible benefits of using a slew maneuver have been discussed for imaging satellites, see for example [6]. Slew maneuvers for satellites are usually deployed for a specific reason, such as the need for a particular sensor, often a camera, to track an area of interest. The method can also be used to compensate for the Earth's rotation, essentially pointing the satellite towards a fixed point on the ground in a "spotlight mode" [7].

The mission design for the HYPSO-1 [8] stipulates a single-axis slew maneuver to improve the data gathered by its payload. The HYPSO-1 CubeSat carries a push-broom hyperspectral imager as its main payload, which produces hyperspectral data cubes. The slew maneuver is intended to let subsets of the resulting image, henceforth called scan-lines, overlap with each other along track, so that techniques such as super-resolution can increase the utility of the down-linked data [9], [10].

The contribution of this paper is the analysis of data collected during a slew maneuver performed by the HYPSO-1 satellite. The accuracy of the selected slew maneuver is evaluated in the context of images taken by the satellite in the first months of operation. The performance is measured by looking at raw data from the hyperspectral camera for two different images of the same location, showing how the HYPSO-1 slew maneuver can be used to decrease the ground sampling distance (GSD) and, consequently, increase the number of samples per area within the target region.

Section II describes the theory and methods used: both the slew maneuver, including the coordinate frames, and the performance metrics are defined. Section III describes the hyperspectral imager of the HYPSO-1 mission and the observation campaign conducted to obtain the data used in this paper. Section IV presents the data from the campaign, with accompanying calculations and the evaluation. The results are discussed in Section V, and Section VI concludes the paper.

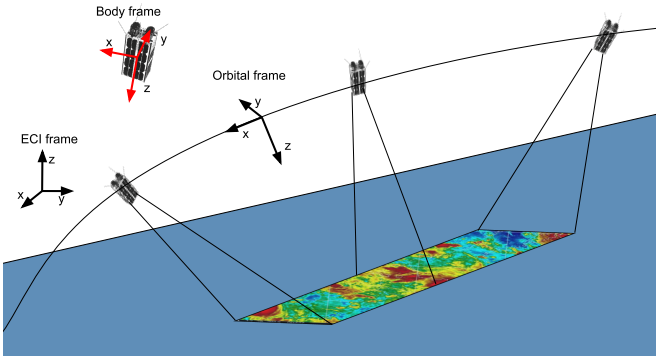

Fig. 1: The HYPSO-1 slew maneuver. Three coordinate frames are depicted: the body frame, the orbital frame (the LVLH frame), and the inertial (ECI) frame. The satellite moves from right to left in the figure as it images the area of interest.

II. Theory

Three coordinate frames are relevant to the slew maneuver: the inertial reference frame, i, the orbital reference frame, o, and the satellite body frame, b, see Figure 1. For the satellite

*The work is partly sponsored by the Research Council of Norway through the Centre of Excellence funding scheme, grant number 223254 (AMOS), the HYPSCI grant number 325961, and has received funding from the NO Grants 2014 – 2021, under Project ELO-Hyp, contract no. 24/2020.

[1,2] The authors are with the Norwegian University of Science and Technology, NO-7491 Trondheim, Norway.

† B. A. Kristiansen and D. D. Langer contributed equally to this work and should be considered co-first authors.

[1] B. A. Kristiansen, J. L. Garrett, S. Berg, J. T. Gravdahl, and T. A. Johansen are with the Department of Engineering Cybernetics at NTNU. E-mails: {bjorn.a.kristiansen, joseph.garrett, jan.tommy.gravdahl, tor.arne.johansen}@ntnu.no, simbe@stud.ntnu.no,

[2] D. D. Langer is with the Department of Marine Technology at NTNU. E-mail: dennis.d.langer@ntnu.no,

body frame, the axes coincide with the main axes of intertia of the satellite, with, most notably, the z-axis pointing out through the side where the hyperspectral imager is pointing. The orbital reference frame is a local vertical, local horizontal (LVLH) reference frame with the z-axis pointed towards nadir. The x-axis of the orbital reference frame points in the velocity direction, and the y-axis completes the right-handed coordinate system. The LVLH frame can then expressed as

$$\hat{\mathbf{x}}_o^i = \frac{\mathbf{v}^i}{||\mathbf{v}^i||}, \quad \hat{\mathbf{z}}_o^i = -\frac{\mathbf{r}^i}{||\mathbf{r}^i||}, \quad \hat{\mathbf{y}}_o^i = \frac{\hat{\mathbf{z}}_o^i \times \hat{\mathbf{x}}_o^i}{||\hat{\mathbf{z}}_o^i \times \hat{\mathbf{x}}_o^i||}, \tag{1}$$

where $\hat{\mathbf{x}}_o^i$, $\hat{\mathbf{y}}_o^i$, and $\hat{\mathbf{z}}_o^i$ denote the orthogonal unit vectors for the LVLH reference frame, $\mathbf{r}^i$ and $\mathbf{v}^i$ are the position and velocity vectors represented in the inertial frame, respectively, and $\times$ is the vector cross product, required for completing the right handed coordinate system.

During the slew maneuver, the angular velocity of the satellite relative to the orbit frame is controlled. This angular velocity can be calculated as [11]

$$\boldsymbol{\omega}_{ob}^b = \boldsymbol{\omega}_{ib}^b - \boldsymbol{\omega}_{io}^b = \boldsymbol{\omega}_{ib}^b - \mathbf{R}_i^b \boldsymbol{\omega}_{io}^i, \tag{2}$$

where $\boldsymbol{\omega}_{io}^b$ is the angular velocity of the orbit frame relative to the inertial frame, $\boldsymbol{\omega}_{ib}^b$ is the angular velocity of the body frame relative to the inertial frame, both represented in body frame and $\mathbf{R}_i^b$ is the rotation matrix from orbit frame to body frame. The angular velocity of the orbit frame relative to the inertial frame, represented in the interial frame, $\boldsymbol{\omega}_{io}^i$, is defined in [12] as

$$\boldsymbol{\omega}_{io}^i = \frac{\mathbf{r}^i \times \mathbf{v}^i}{(\mathbf{r}^i)^\intercal \mathbf{r}^i}. \tag{3}$$

Equation (3) is changed slightly compared to [12] because the quaternion between the inertial and the body frame is available in the telemetry, making it possible to compute $\mathbf{R}_i^b$ directly.

Note that (2) is necessary since $\boldsymbol{\omega}_{ob}^b$ is not directly measured, as the IMU will measure $\boldsymbol{\omega}_{ib}^b$. Using the estimated position and velocity, $\mathbf{r}^i$ and $\mathbf{v}^i$, in addition to the estimated values for $\boldsymbol{\omega}_{ib}^b$ based on sensor measurements, we can find an estimate for $\boldsymbol{\omega}_{ob}^b$ through the relationships in (2) and (3). Maneuvers on the HYPSO-1 satellite are implemented using PD controllers, see e.g. [13].

For the accuracy measurements we use a root-mean-square deviation (RMSD) measure, for convenience given here as

$$RMSD = \sqrt{\frac{1}{T}\sum_{t=1}^{T}(x_{\text{ref},t} - x_t)^2}, \tag{4}$$

where T is the number of time steps, x_t is the reference value at the given time step and $x_{\text{ref},t}$ is the corresponding reference value. For the attitude accuracy, the "root square deviation" part of (4) is replaced, resulting in

$$\text{Accuracy}_{\text{quaternion}} = \frac{1}{T}\sum_{t=1}^{T} \arccos\left(|\mathbf{q}_t^\intercal \mathbf{q}_{\text{ref},t}|\right), \tag{5}$$

where $\arccos\left(|\mathbf{q}_t^\intercal \mathbf{q}_{\text{ref},t}|\right)$ is a distance metric on SO(3) [14], and $\mathbf{q}_t$ and $\mathbf{q}_{\text{ref},t}$ are the quaternion and quaternion reference for a given time step, respectively.

There exist several spatial resolution metrics to characterize imagery [15], [16]. Among them is the ground sampling distance (GSD), which is expected to be decreased by the slewing maneuver. [15] describes GSD as *pixel pitch projected onto ground plane*. Pixel pitch is the the distance from pixel center to pixel center of two consecutive pixels in an image. For a push broom scanning system, GSD can be drastically different in the two dimensions of an image, along-track and across-track. This paper focuses on along-track GSD.

III. Experimental setup

The attitude control system of the HYPSO-1 satellite, based on the NanoAvionics M6P satellite bus, is equipped with reaction wheels and magnetorquers as well as inertial measurement unit, global navigation satellite system receiver and startracker for navigation. HYPSO-1 is a 6U CubeSat ($10 \times 20 \times 30$ cm) with about 7 kg mass. The reaction wheels are the main actuators used for attitude control, meaning they produce the torque required to perform the pointing of the hyper-spectral imager towards targets on the ground, and to perform the slewing maneuver. The magnetorquers are used to de-saturate the reaction wheels. For more information on the imager itself and its performance, see [17], [18].

There are several ways to change the GSD, for example by changing the framerate. Here the framerate is kept constant in order to inspect the impact of the slewing maneuver itself.

Two images targeting the same location are taken. Both images are captured when HYPSO-1 is passing over the location of interest close to zenith. One image is captured using a nadir pointing maneuver, and the other using a slewing maneuver. For the nadir pointing maneuver, the reference was given in terms of a unit quaternion as $\mathbf{q}_b^o = [0.99871, -0.036528, 0.035297, 0]^\intercal$, specifying body frame orientation relative to the orbit frame. Note that the unit quaternion is denoted with the scalar part first, followed by the three components that make up the vector part. Also note that the pointing is not precisely nadir, but offset by about $5.8°$. For simplicity, the maneuver will still be referred to as the nadir pointing maneuver for the remainder of this paper.

The angular velocity about the orbit frame y-axis, the reference for the slew maneuver, is given in terms of initial and final nadir angle of $10°$ and $-10°$. A slew duration of 43.45 seconds yields an angular velocity reference of $\boldsymbol{\omega}_{ob,\text{ref}}^b = [0, -0.0080329, 0]^\intercal \text{rad/s}$. Note that the reference is different from the nominal slew maneuver defined in [8]. The start and end attitude of the slewing maneuver minimally affect the slew as the current implementation moves the transient periods of the angular velocity response outside the specified slew duration.

The nadir pointing image was taken on Saturday July 16 at 08:29:00 UTC, and the slewing maneuver image was taken on Sunday July 24 at 08:30:33 UTC, both in 2022. The target area for both of the maneuvers on the ground were a part of the coastal area where Romania meets the Black Sea.

IV. Results

Figure 2 shows the two RGB representations of the hyperspectral data cubes manually georeferenced over a topographic map, with the image taken by the nadir pointing maneuver to the left and the image taken during slew maneuver

to the right. Note the difference in area covered by the two maneuvers. A zoom-in of a common section of both images is shown in Figure 3, again with the nadir image on the left and the slewing maneuver on the right. The images have been bilinearly resampled to the same scale, and the contrast has been enhanced to easier differentiate between the details in each picture.

Fig. 2: Nadir pointing (left) and slew (right) RGB images overlayed on topographical map (OpenStreetMap).

Fig. 3: Nadir pointing (left) and slew (right) RGB images over the port of Constanța, Romania. Zoom-in on the images in Figure 2, bilinearly resampled to the same scale with contrast enhanced.

Figure 4 shows the ADCS telemetry derived satellite pose in 3D space. The figure also shows a latitude-longitude grid representing the Earth with coordinates labels, the satellite orbital and ground track, the footprint of the images captured during the maneuver, and lines indicating the pointing direction during image capture. Note the difference in pointing direction between the two captures.

The telemetry includes the attitude represented as a unit quaternion $\mathbf{q}_b^i$, the angular velocity $\boldsymbol{\omega}_{ib}^b$, the position $\mathbf{r}^i$, and the velocity $\mathbf{v}^i$, all estimated onboard. They are shown in Figure 5 for the nadir pointing capture. The accuracy for

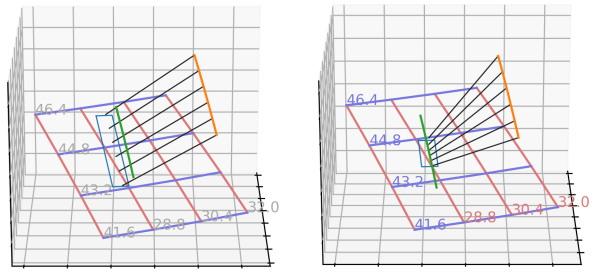

(a) Pointing geometry of nadir capture.

(b) Pointing geometry of slew capture.

Fig. 4: Capture pointing geometry inferred from ADCS telemetry. Orange: Satellite track in ECI. Green: Satellite ground track. Blue rectangle: Image ground footprint. Black lines: z-axis direction at 6 uniformly spaced points in time during image capture. Light red: lines of constant longitude. Light blue: Lines of constant latitude.

the nadir pointing maneuver, using (5) is taken during the maneuver itself, as marked with the shaded area starting at time zero in the figures. The accuracy of the nadir pointing maneuver is $0.00114 \text{ rad} = 0.0653°$, computed using (5), see Table I.

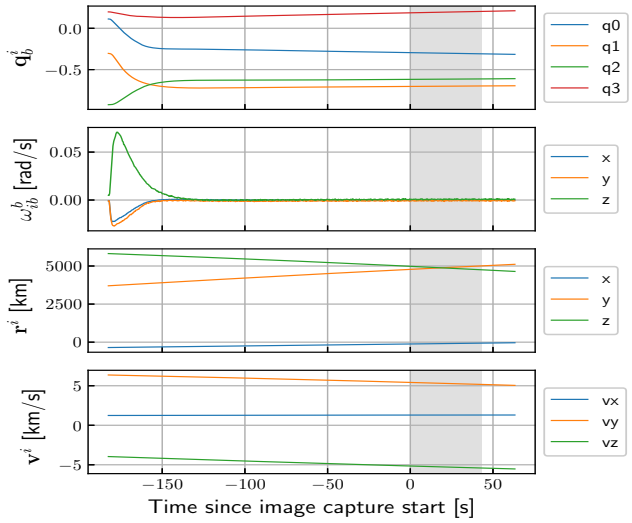

Fig. 5: Telemetry from the spacecraft when pointing nadir. From top to bottom: $\mathbf{q}_b^i$, $\boldsymbol{\omega}_{ib}^b$, $\mathbf{r}^i$, and $\mathbf{v}^i$. Gray area indicates the time period when HYPSO-1 was recording data.

Figure 6 shows the LVLH quaternion $\mathbf{q}_b^o$ during the image capture. To construct $\mathbf{q}_b^o$, $\mathbf{q}_o^i$ is inferred from the attitude information for $\mathbf{q}_b^i$, shown in Figure 5, and the definition of the LVLH coordinate system in (1).

For the slew maneuver, the telemetry is displayed in Figure 7. Note that the satellite prepares the slew maneuver by spinning up to a constant angular rate ahead of the defined start of the maneuver, thus moving the transient outside of the image capture period. $\boldsymbol{\omega}_{ob}^b$, the angular velocity of the body relative to the orbit frame, is computed based on the

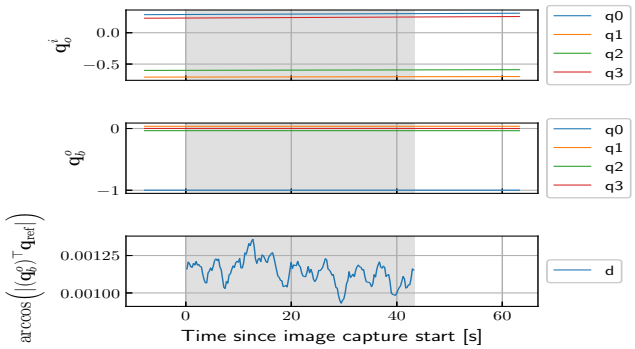

Fig. 6: Attitude information from the nadir pointing maneuver during image capture. Quaternion representing the attitude of the axes of the LVLH frame relative to the inertial frame $\mathbf{q}_o^i$, the attitude of the body axes relative to the LVLH frame $\mathbf{q}_b^o$, and the distance from the reference quaternion used in (5), given in radians.

telemetry calculated by (2) and shown in Figure 8. Figure 8 also displays $\boldsymbol{\omega}_{io}^b$, albeit given in a different frame than in (3) for easier comparison to the other measurements in the figure. Note that $\boldsymbol{\omega}_{ib}^b$ and $\boldsymbol{\omega}_{ob}^b$ are very similar in Figure 8 due to the magnitude of $\boldsymbol{\omega}_{ib}^b$ being larger than that of $\boldsymbol{\omega}_{io}^b$. The last part of the figure shows the control error during the image capture period. The accuracy of the slew maneuver in terms of RMSD between the signal and the reference for the angular velocity during capture is shown in Table I. It has three components, one for each component of the $\boldsymbol{\omega}_{ob}^b$ vector. The y-component is the axis around which the slew rotation takes place. That all three components are approximately the same magnitude signifies that the satellite manages to hold the reference in all three axes equally well.

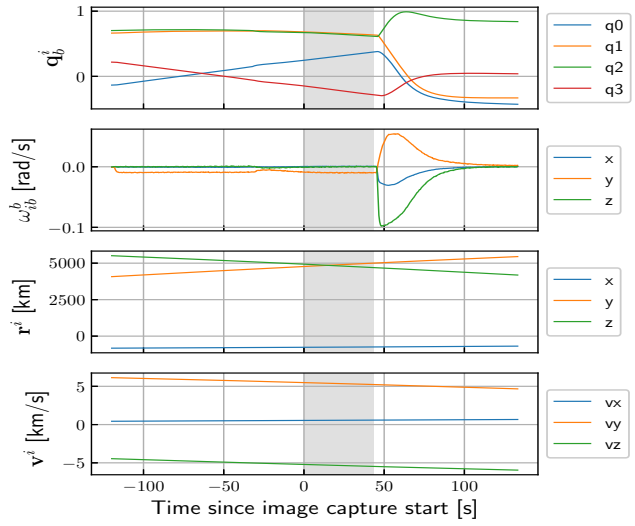

Fig. 7: Telemetry from the ADCS before, during and after the slew maneuver. From top to bottom: $\mathbf{q}_b^i$ $\boldsymbol{\omega}_{ib}^b$, $\mathbf{r}^i$, and $\mathbf{v}^i$. Gray area indicates the time period when HYPSO-1 was recording data.

TABLE I: Accuracy measurements for the two maneuvers.

Capture	**Accuracy**
Pointing	1.14 mrad
Slew	$[0.6347, 0.6752, 0.4551]^\intercal$ mrad/s

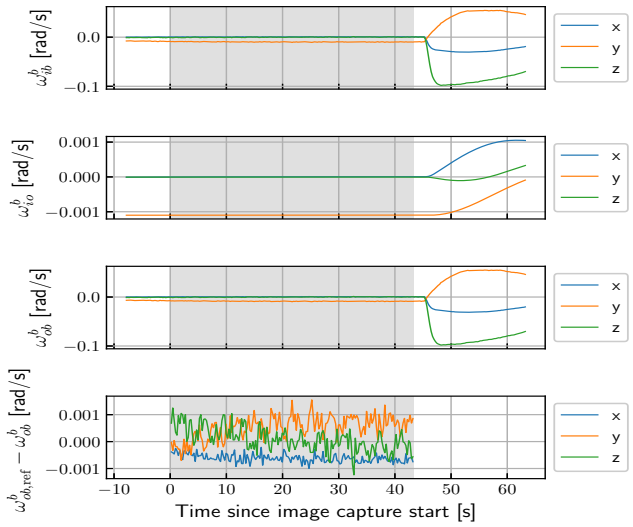

Fig. 8: From top to bottom: $\boldsymbol{\omega}_{ib}^b$ from telemetry, $\boldsymbol{\omega}_{io}^b$ from (2) and (3), $\boldsymbol{\omega}_{ob}^b$ from (3), and the control error $\boldsymbol{\omega}_{ob,\text{ref}}^b - \boldsymbol{\omega}_{ob}^b$. Gray area indicates the time period when HYPSO-1 was recording data.

Figure 9 shows the GSD along track in the center of the swath for the pointing and slewing captures. Noise in the sensors translates into noise of the GSD estimation. Table II shows that the area covered by the image taken during the nadir pointing maneuver covers more than twice as large an area as the image taken during the slewing maneuver. Table II also shows the mean GSD over all scan-lines. The decrease from 321.6 m to 117.0 m signifies a 63.6% reduction. The fourth column in Table II shows how many pixel samples are contained in the region bounded by the orange rectangle shown in Figure 2, containing an area of 192 km^2. The region contains 64.3% less samples for the image taken during pointing compared to slewing. The increased density of pixels correlates with an increase in the signal, or the amount of light collected, per unit area.

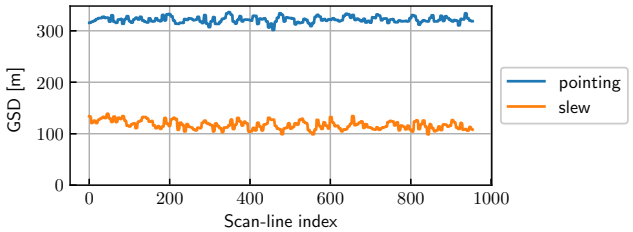

Fig. 9: Ground-sampling-distance along the scanning direction for nadir pointing and slew maneuver.

TABLE II: Figures of interest for the two captures.

Capture	**mean GSD**	**ca. Area [km^2]**	**Pixels in region**
Pointing	321.6 m	13726	1825
Slew	117.0 m	4959	5117

V. Discussion

There are several steps used to acquire the data presented in this paper, giving us four possible error sources. The four stages are 1) generating a reference, 2) estimating the attitude, 3) controlling the attitude towards the reference, and 4) possible error sources related to the hyperspectral imager. The first error source, generating a reference, might be slightly offset compared to our desired reference if the model we use to calculate where we want to point is not accurate enough. In addition, the time where the maneuver starts has to be specified: while a small error here might give a large deviation in the image, it would not change the accuracy results we got using the performance metrics introduced in Section II, as they are indifferent to what scene that the imager captures. The control system will not be able to control the satellite towards the reference attitude exactly, but with an error that is required to within a small bound, see [8]. The same can be said for the estimated variables. There is a possibility that error source 4), errors with the imager, also influences the final images. However, these errors should be static, meaning that they should be identical between the various images. Error source 1) can possibly vary depending on location.

Using the results from the telemetry we can see from the accuracy of the pointing maneuver and the slewing maneuver that the ADCS manages to control the satellite towards its references, making error source 3 small. As the images show what we expect to see, we may conclude that the compound errors from the four mentioned sources are small.

The basic idea behind the concept of operations for the HYPSO-1 satellite is that it performs a slew maneuver such as the one performed in this paper to acquire push-broom hyper-spectral images. From the results in this paper we can see that the attitude control objectives are met with some accuracy during the duration of the image captures. The distance from the reference attitude for nadir pointing is, as shown in Figure 6, very low, making it a good comparison for the slew maneuver when looking at the science results. As Table II shows, the mean GSD of the slew maneuver is decreased by 2/3 relative to the image taken during the pointing maneuver. This measure sets a limit for how much the image can be improved by post-processing algorithms, and thus it can be argued that the use of this slewing maneuver helps increase the limit for how much information can be gathered.

VI. Conclusion

The slew maneuver of the HYPSO-1 satellite performs well according to the accuracy measures used in this paper. Moreover, the slew maneuver increases the number of photons that are detected per area of the hyperspectral image, by decreasing the GSD. This suggests that the slew maneuver produces images that can be exploited through image restoration, deconvolution, and super-resolution image processing algorithms (e.g. [19]) to increase the utility of the HYPSO-1 data products.

Acknowledgment

The authors would like to thank Sivert Bakken and representatives of NanoAvionics for valuable discussions.

References

[1] B. A. Kristiansen, M. E. Grøtte, and J. T. Gravdahl, "Quaternion-Based Generalized Super-Twisting Algorithm for Spacecraft Attitude Control," *IFAC-PapersOnLine*, vol. 53, no. 2, pp. 14 811–14 818, 2020.

[2] M. E. Grøtte, J. T. Gravdahl, T. A. Johansen, J. A. Larsen, E. M. Vidal, and E. Surma, "Spacecraft Attitude and Angular Rate Tracking using Reaction Wheels and Magnetorquers," *IFAC-PapersOnLine*, vol. 53, no. 2, pp. 14 819–14 826, 2020.

[3] E. Sin, S. Nag, V. Ravindra, A. Li, and M. Arcak, "Attitude Trajectory Optimization for Agile Satellites in Autonomous Remote Sensing Constellations," *AIAA Scitech 2021 Forum*, Jan. 2021.

[4] K.-S. Kim and Y. Kim, "Robust backstepping control for slew maneuver using nonlinear tracking function," *IEEE Transactions on Control Systems Technology*, vol. 11, no. 6, pp. 822–829, Nov. 2003.

[5] J. Li, M. Post, and R. Lee, "Real-Time Nonlinear Attitude Control System for Nanosatellite Applications," *Journal of Guidance, Control, and Dynamics*, vol. 36, no. 6, pp. 1661–1671, Nov. 2013.

[6] M. A. Cutter, D. R. Lobb, and R. A. Cockshott, "Compact High Resolution Imaging Spectrometer (CHRIS)," *Acta Astronautica*, vol. 46, no. 2, pp. 263–268, Jan. 2000.

[7] H. Kim and Y. K. Chang, "Mission scheduling optimization of SAR satellite constellation for minimizing system response time," *Aerospace Science and Technology*, vol. 40, pp. 17–32, Jan. 2015.

[8] M. E. Grøtte, R. Birkeland, E. Honoré-Livermore, S. Bakken, J. L. Garrett, E. F. Prentice, F. Sigernes, M. Orlandić, J. T. Gravdahl, and T. A. Johansen, "Ocean Color Hyperspectral Remote Sensing With High Resolution and Low Latency—The HYPSO-1 CubeSat Mission," *IEEE Transactions on Geoscience and Remote Sensing*, vol. 60, pp. 1–19, 2021.

[9] J. L. Garrett, D. Langer, K. Avagian, and A. Stahl, "Accuracy of super-resolution for hyperspectral ocean observations," in *IEEE/MTS OCEANS, Marseille*, 2019.

[10] J. L. Garrett, S. Bakken, E. F. Prentice, D. Langer, F. S. Leira, E. Honoré-Livermore, R. Birkeland, M. E. Grøtte, T. A. Johansen, and M. Orlandić, "Hyperspectral image processing pipelines on multiple platforms for coordinated oceanographic observation," in *IEEE WHISPERS*, 2021.

[11] O. Egeland and J. T. Gravdahl, *Modeling and simulation for automatic control*. Marine Cybernetics Trondheim, Norway, 2002.

[12] E. Oland and R. Schlanbusch, "Reaction wheel design for CubeSats," in *Int Conf Recent Adv Inf Technol*, Jun. 2009, pp. 778–783.

[13] J.-Y. Wen and K. Kreutz-Delgado, "The attitude control problem," *IEEE Trans Automat*, vol. 36, no. 10, pp. 1148–1162, Oct. 1991.

[14] D. Q. Huynh, "Metrics for 3D Rotations: Comparison and Analysis," *J Math Imaging Vis*, vol. 35, no. 2, pp. 155–164, Oct. 2009.

[15] Álvaro Q. Valenzuela and J. C. G. Reyes, "Basic spatial resolution metrics for satellite imagers," *IEEE Sensors Journal*, vol. 19, no. 13, pp. 4914–4922, 2019.

[16] D. D. Langer, T. A. Johansen, and J. S. A, "Consistent along track sharpness in a push-broom imaging system," in *IGARSS 2023 - IEEE International Geoscience and Remote Sensing Symposium*, 2023.

[17] E. F. Prentice, M. E. Grøtte, F. Sigernes, and T. A. Johansen, "Design of a hyperspectral imager using COTS optics for small satellite applications," in *ICSO 2020*, vol. 11852. SPIE, Jun. 2021, pp. 2154–2171.

[18] S. Bakken, M. B. Henriksen, R. Birkeland, D. D. Langer, A. E. Oudijk, S. Berg, Y. Pursley, J. L. Garrett, F. Gran-Jansen, E. Honoré-Livermore, M. E. Grøtte, B. A. Kristiansen, M. Orlandic, P. Gader, A. J. Sørensen, F. Sigernes, G. Johnsen, and T. A. Johansen, "Hypso-1 cubesat: First images and in-orbit characterization," *Remote Sensing*, vol. 15, no. 3, 2023.

[19] R. C. Gonzalez and R. E. Woods, *Digital image processing*, 4th ed. Pearson, 2018.